Research Square

Preprints are preliminary reports that have not undergone peer review.
They should not be considered conclusive, used to inform clinical practice,
or referenced by the media as validated information.

Surrogate Modelling of Tyre-Pavement Interaction Under Tractive Loading

Débora Cardoso da Silva

sdeboracardoso@outlook.com

Univ. Limoges

Ndrianary Rakotovao Ravahatra

Univ. Limoges

Sylvie Yotte

Univ. Limoges

Benoit Picoux

Univ. Limoges

Philippe Reynaud

Univ. Limoges

Christophe Petit

Univ. Limoges

Research Article

Keywords:

Posted Date: November 25th, 2026

DOI: https://doi.org/10.21203/rs.3.rs-11384777/v1

License: This work is licensed under a Creative Commons Attribution 4.0 International License.
Read Full License

Additional Declarations: No competing interests reported.

Surrogate Modelling of Tyre-Pavement Interaction Under Tractive Loading

Débora Cardoso da Silva[1*], Ndrianary Rakotovao Ravahatra[1], Sylvie Yotte[1], Benoit Picoux[1], Philippe Reynaud[1], Christophe Petit[1]

[1]Univ. Limoges, GC2D, UR 14447, F-87000, Limoges, France.

*Corresponding author(s). E-mail(s): sdeboracardoso@outlook.com;
Contributing authors: ndrianary.rakotovao-ravahatra@unilim.fr; sylvie.yotte@unilim.fr; benoit.picoux@unilim.fr; philippe.reynaud@unilim.fr; christophe.petit@unilim.fr;

Abstract

Purpose: Tyre-pavement tractive contact governs stress states associated with surface-initiated pavement damage. Conventional numerical methods can accurately estimate these stresses but remain computationally prohibitive for industrial applications and uncertainty propagation. This study develops a computationally efficient surrogate modelling framework for predicting pavement-surface strain fields under braking and investigates the influence of input-parameter uncertainty on critical strain responses.

Methods: A polynomial response surface is trained using a synthetic dataset generated with an enriched central composite design and a fast semi-analytical tyre–pavement contact model. Surrogate accuracy is assessed through five-fold cross-validation. The trained model is subsequently used for uncertainty propagation and global sensitivity analysis.

Results: The surrogate achieves high predictive accuracy, with R^2 above 0.83 for 95% of the spatial nodes and standardised RMSE below 0.03 for 75% of the nodes on out-of-sample data. Once trained, it evaluates the complete surface strain field in approximately 4 ms. Critical strains are concentrated beneath the tyre contact patches and are primarily associated with high vertical loads and low surface-course elastic modulus, with moderate sensitivity to the friction coefficient and surface-course Poisson's ratio.

Conclusion: The proposed framework enables efficient uncertainty and sensitivity analyses of pavement near-surface responses. It identifies key loading, material, and surface properties that should be prioritised for reliable assessment of pavement performance under tractive loading.

Keywords: Response surface, Semi-analytical contact model, Uncertainty propagation, Braking, Dual tyres

Acknowledgements. The authors gratefully acknowledge Dr. Arnaud Duval, Dr. Thibaut Chaise, and Dr. Daniel Nelias from the Laboratoire de Mécanique des Contacts et des Structures (LaMCoS), INSA Lyon, for their advice and support with the semi-analytical contact model. D. Cardoso da Silva was supported by a doctoral contract at the University of Limoges.

1 Introduction

Surface-initiated cracking in asphalt pavements has been associated with the complex and localized stress states generated at the tyre–pavement interface [1]. Conventional pavement design methods, however, typically represent tyre loading as a uniformly distributed vertical pressure over a simplified contact patch, thereby neglecting the non-uniform and three-dimensional nature of actual contact stresses. Indeed, field measurements conducted in the late 1990s [2] demonstrated that contact stresses beneath actual truck tyres are highly non-uniform and exhibit substantial shear components. Subsequent investigations have shown that the assumption of a uniform contact pressure can significantly underestimate susceptibility to near-surface distress [3] or, in certain configurations, overestimate vertical strains [4]. More broadly, realistic tyre profiles generate stress distributions that differ markedly from those produced by uniform loading, particularly near the pavement surface [5].

Tyre–pavement interaction becomes particularly critical during vehicle manoeuvres that induce significant tangential loads [3, 4, 6]. Specifically, braking and acceleration generate elevated longitudinal shear stresses [7], an effect that may be further amplified by a higher friction coefficient between the tyres and pavement [8]. Consequently, braking conditions have been associated with increased cracking damage potential for both surface-initiated [6] and bottom-up fatigue cracking [4]. However, capturing full three-dimensional contact stress fields experimentally under tractive loading remains technically challenging and resource-intensive.

To overcome these experimental limitations, numerical modelling has become an established approach for evaluating tyre–pavement contact, notably through the finite element method (FEM) [3, 6, 8–10]. FEM provides considerable flexibility for modelling complex tyre geometries and nonlinear, time-dependent material constitutive laws; however, a single simulation can require tens of CPU hours [9]. To reduce this computational burden, alternative approaches have emerged, including hybrid FEM–Discrete Element Method (DEM) frameworks [11] and semi-analytical contact models [12–14].

Surrogate modelling addresses this computational bottleneck by replacing an expensive high-fidelity solver with a low-cost mathematical emulator. This capability is particularly valuable for uncertainty propagation and global sensitivity analyses, which may require hundreds of thousands to millions of model evaluations with varying inputs. Recent advances in surrogate-assisted mechanistic pavement analysis have relied primarily on machine learning approaches applied to FEM databases, including artificial neural networks [15], generative adversarial networks [16, 17], Bayesian neural networks [18], and graph neural networks [19]. These FEM-trained surrogates can provide accurate predictions and reduce evaluation times to a few seconds, but database generation costs remain high.

Despite these developments, the use of computationally efficient contact models coupled with surrogate modelling frameworks for large-scale uncertainty propagation and sensitivity analysis remains underexplored [20]. A fast contact model offers a distinct advantage: it substantially reduces database-generation costs while providing direct control over the sampling strategy for the training and test data.

In this work, we develop a surrogate modelling framework for predicting pavement-surface strain fields under severe braking. The framework employs an interpretable polynomial response surface trained on a database generated using an enriched central composite design and a fast semi-analytical contact solver. The framework is subsequently used to identify the (1) most influential input parameters, (2) quantify the variability of the predicted strain fields, and (3) determine critical parameter combinations associated with severe responses.

The remainder of this paper is organised as follows. Section 2 details the reference semi-analytical contact model and outlines the investigated case study. Section 3 describes the surrogate development and sampling design. Finally, Section 4.1 evaluates surrogate accuracy, Section 4.2 presents the global sensitivity analysis, and Section 4.3 examines the maximum strain responses and their relationship with input parameter variability under braking.

2 Numerical modelling framework

The numerical modelling framework comprises the semi-analytical model used to simulate tyre–pavement interaction and evaluate the strain response of interest, together with the main assumptions adopted for the case study.

2.1 Reference contact model

The pavement-surface strain field is evaluated using a computationally efficient semi-analytical model (SAM) based on elementary solutions from contact mechanics. The model is applicable to non-conformal contact problems involving arbitrary geometries and multidirectional external loadings. The bodies are represented as elastic half-spaces discretised on a regular rectangular grid, under the assumption of small elastic displacements. Figure 1 illustrates the overall numerical framework. The origin of the coordinate system is positioned at the centre of the contact area, with the x-axis aligned with the longitudinal (rolling) direction and the y-axis with the lateral direction.

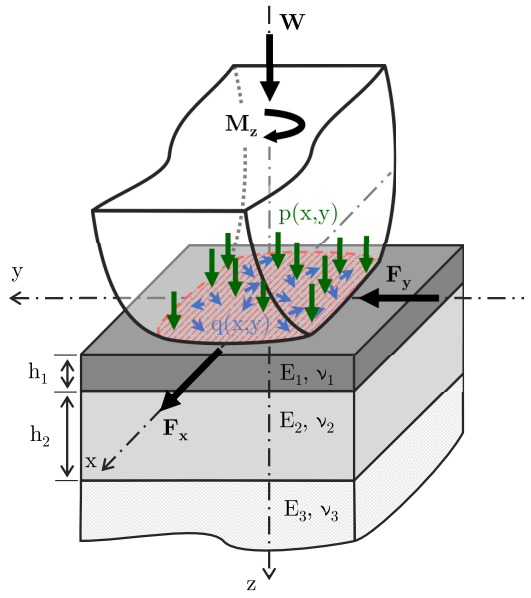

Fig. 1 Schematic of the rolling contact problem: coordinate frames, applied loading (W, F_x, F_y), spinning moment (M_z), and interfacial contact stresses (p, q). Adapted from Wallace et al. [21].

SAM formulates the contact problem as a constrained minimisation of the complementary energy, subject to non-adhesion and Coulomb friction constraints. The variational formulation follows the framework developed by Kalker for tractive rolling contact in linear elasticity [22]. The minimisation problem is solved efficiently using the Conjugate Gradient Method (CGM) [23, 24].

The contact problem is partitioned into normal and tangential components, which are solved sequentially within an iterative loop. The normal contact problem is governed by the equilibrium between the total applied vertical load W and the contact pressure $p(x, y)$ over the contact zone Γ_c:

$$W = \iint_{\Gamma_c} p(x, y)\, \mathrm{d}x\, \mathrm{d}y \tag{1}$$

subject to the non-adhesion condition $p(x, y) \geq 0$.

The tangential contact problem accounts for the applied longitudinal force F_x, lateral force F_y, and spinning moment M_z through the corresponding global equilibrium equations presented in Equation 2, where $\mathbf{q} = (q_x, q_y)^{\mathrm{T}}$ denotes the shear contact stress vector.

$$F_x = \iint_{\Gamma_c} q_x(x, y)\, \mathrm{d}x\, \mathrm{d}y, \tag{2a}$$

$$F_y = \iint_{\Gamma_c} q_y(x, y)\, \mathrm{d}x\, \mathrm{d}y, \tag{2b}$$

$$M_z = \iint_{\Gamma_c} \left[x q_y(x, y) - y q_x(x, y)\right]\, \mathrm{d}x\, \mathrm{d}y \tag{2c}$$

The local shear stresses are bounded by the Coulomb friction law:

$$\|\mathbf{q}\| \leq \mu p \tag{3}$$

where μ represents the surface friction coefficient.

The elastic displacement u_α, with $\alpha \in \{x, y, z\}$, is obtained from the contact stress distribution through spatial convolution with the corresponding Green functions. These functions describe the displacement response at an observation point (x, y, z) due to a unit point load applied at a source point $(x', y', 0)$. For instance, the contribution of the applied pressure field to the elastic displacement is written as:

$$u_\alpha^p(x,y,z) = \iint_{-\infty}^{+\infty} G_\alpha^p(x-x', y-y', z)p(x', y')\mathrm{d}x'\mathrm{d}y' \tag{4}$$

where G_α^p denotes the Green function associated with the normal contact stress p. Similar convolution relations are used for the tangential contact stresses, whose contributions are superposed according to the principle of linear superposition. For the multilayered structures considered in this study, the Green functions are derived using Papkovich-Neuber potentials [21, 25]. The two-dimensional spatial convolutions are evaluated efficiently using the discrete Fast Fourier Transform (DC-FFT).

The SAM framework has previously been validated against experimental measurements of contact pressure [5] and longitudinal and transverse strains recorded at different depths in a full-scale pavement test facility [26]. Furthermore, its performance has been successfully benchmarked against FEM contact models [27]. Its exceptional computational efficiency enables the generation of the extensive training databases required for surrogate model development.

2.2 Case study

The present study investigates a critical driving condition characterised by severe braking. The analysis focuses on the tensile strain response at the surface of a flexible pavement, considering a detailed geometrical representation of a dual-tyre assembly.

2.2.1 Strain criterion for surface damage

The surrogate model is developed to predict the spatial distribution of the equivalent strain field, denoted by $\hat{\varepsilon}$. This response variable is based on a crack-initiation criterion rooted in continuum damage mechanics [28], which provides a scalar measure of the local strain state under multidirectional loading. The criterion assumes that micro-crack initiation is driven primarily by positive (tensile) principal strains:

$$\hat{\varepsilon} = \sqrt{\langle\varepsilon_1\rangle_+^2 + \langle\varepsilon_2\rangle_+^2 + \langle\varepsilon_3\rangle_+^2}, \tag{5}$$

where ε_i ($i \in \{1,2,3\}$) denote the principal strain components, and $\langle\cdot\rangle_+$ represents the Macaulay bracket, defined as:

$$\langle\varepsilon_i\rangle_+ = \frac{\varepsilon_i + |\varepsilon_i|}{2} \tag{6}$$

For conciseness, the present study focuses on the equivalent strain response evaluated at the pavement surface. However, the proposed surrogate-modelling methodology is versatile and can be applied analogously to other spatial fields throughout the pavement structure.

2.2.2 Tyre properties

A dual-tyre set (295/65R22.5) is considered for all numerical simulations. The actual tyre geometry, inflated to 820 kPa, was reconstructed from high-resolution laser-scanning data and discretized into a regular mesh with a grid spacing of 5 mm [29]. This resolution corresponds to approximately one-eighth of a typical tread-block width and provides a sufficiently detailed representation of the tread pattern. Figure 2 illustrates the reconstructed geometrical model.

The tyres are modelled as a three-layer structure with an elastic half-space, a thin and stiff belt layer representing the nylon and steel reinforcements, and a tread rubber layer. The reinforcement layer constrains tread distortion under vertical loading, refining the predicted footprint shape. The layers are assumed to have uniform thickness and perfect inter-layer bonding, exhibiting linear elastic behaviour. The structural parameters and material properties of the tyre model are summarised in Table 1.

2.2.3 Pavement properties

The pavement structure comprises a dense asphalt concrete wearing course (BBSG), a bituminous-treated road base (GB), and a compacted subgrade. The nominal layer thicknesses follow the French Pavement Design Catalogue [30] for a structure designed to sustain traffic from 6.5 million heavy vehicles (gross weight above 35 kN) over a 20-year design life on a subgrade with good bearing capacity ($10 < \mathrm{CBR} \leq 20$). The pavement layers are modelled as linear elastic media at a reference temperature of 15 °C and a loading frequency of 10 Hz.

Table 1 Dual-tyre structural layers and mechanical properties.

Layer	Thickness [mm]	Young's modulus [MPa]	Poisson's ratio
Elastic half-space	∞	3.7	0.50
Reinforcements	5	10,000	0.30
Rubber	35	4.0	0.50

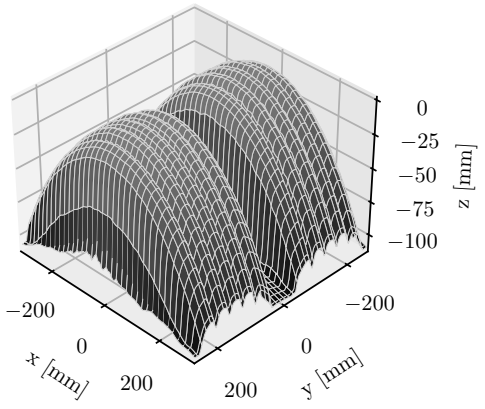

Fig. 2 Reconstructed dual-tyre geometry.

Layer thicknesses and elastic moduli are treated as input variables in the surrogate model to incorporate construction tolerances and material heterogeneity [20]. Their nominal values and assigned probability distributions are detailed in Table 2.

2.2.4 Load condition

The braking condition is simulated by applying a longitudinal tractive force F_x. Because the tyre trajectory is assumed to follow a straight path, lateral forces and spinning moments are neglected ($F_y = 0$ and $M_z = 0$). The longitudinal braking force and vertical axle load W are coupled through the available interface friction. The braking intensity (f_x), or normalised braking force, is defined as the ratio of the mobilised longitudinal force to the Coulomb friction limit μW, such that $F_x = f_x(\mu W)$.

The parameter f_x ranges from 0 (free rolling) to 1 (full slippage). To model severe braking – such as conditions encountered at intersections, steep downhill gradients, or toll plazas [31] – a constant ratio of $f_x = 0.75$ is adopted. This value aligns with the minimum braking-efficiency thresholds mandated for heavy-vehicle homologation in Europe [32].

The vertical load W and friction coefficient μ are varied independently as explanatory variables in the surrogate model to account for their inherent variability, while the braking intensity f_x is kept fixed. The corresponding longitudinal force F_x is then computed deterministically via the relation above.

The vertical load amplitude is defined according to the French Pavement Design Guide [33] and the French Highway Code, which specifies a maximum standard single-axle load of 130 kN with a 5% legal overloading tolerance. The lower bound represents a light-truck axle of approximately 25 kN. The friction coefficient is representative of a dry, dense asphalt surface. The nominal values and variation ranges for all input parameters are summarised in Table 2.

3 Surrogate model development

The surrogate model is developed following the procedure shown in Figure 3. The first step consists of defining the explanatory variables (or features) of the surrogate model, their ranges of variation, and the sampling strategy. The resulting sample points are then used as inputs to the semi-analytical model to generate the responses used for training and validating the surrogate model. Specifically, the response of interest is an equivalent strain criterion evaluated at the pavement surface (Section 2.2.1). The accuracy of the surrogate model is assessed by comparing the reference responses obtained from the semi-analytical model with the corresponding surrogate predictions using a five-fold cross-validation procedure.

3.1 Selection of surrogate-model inputs

It is important to keep the number of independent variables at a manageable level, as it directly affects the dimensionality of the problem. The

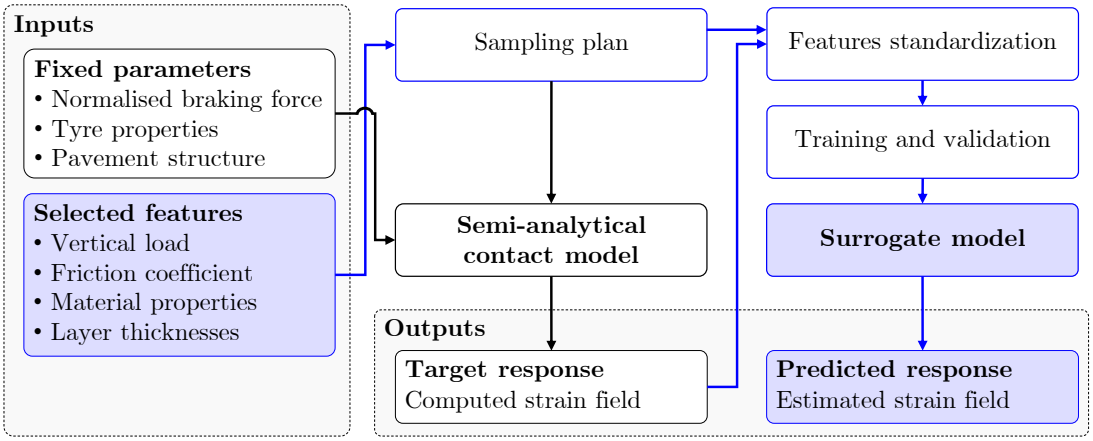

Fig. 3 Surrogate model development flowchart.

assumptions made in Section 2.2 help to reduce the computational effort required. For instance, as the tyre characteristics and braking intensity are assumed to be constant, the surrogate-model inputs comprise $d = 10$ parameters, namely the friction coefficient (μ), the magnitude of the vertical load (W), and the mechanical properties and thicknesses of the pavement layers (E_i, ν_i, h_j, where $i \in \{1, 2, 3\}$ indexes the three pavement layers and $j \in \{1, 2\}$ indexes the two layers whose thicknesses are treated as uncertain). This selection focuses on input parameters in pavement structural design subject to inherent variability.

To define the boundaries of each parameter, a preliminary literature review was conducted to identify the statistical distributions and levels considered for the selected parameters [20], as summarized in Table 2. Where applicable, the global variation ranges are defined based on a specified coverage probability of the corresponding parameter distribution. The selected coverage defines the proportion of the distribution included within the considered range, thereby excluding extreme or unlikely input values. The surrogate model uses these parameters in standardised form, obtained by rescaling their respective ranges to the interval $[-1, +1]$. The corresponding physical values at the coded levels $\{-1, -\ell, 0, +\ell, +1\}$ are also reported in Table 2 and are further discussed in the following section.

3.2 Sampling strategy

A Design of Experiments (DoE) technique, specifically the central composite design (CCD), is employed to sample the parameter space for the development of the surrogate model. Each input parameter, also referred to as a *factor* in the DoE framework, defines one dimension of the standardised parameter space, with its range defined by the coded levels -1 and $+1$. The sampling domain can therefore be represented as a d-dimensional hypercube $\Omega = [-1, +1]^d$.

The CCD generates a set of points in the parameter space that includes a centre point, factorial points, and axial points [34]. Figure 4a illustrates the CCD sampling strategy for a two-dimensional parameter space. The centre point (yellow diamond) corresponds to the midpoint of the parameter ranges, while the factorial points (blue circles) are located at the corners of the parameter space, i.e., all possible combinations of the minimum (-1) and maximum (+1) levels of each factor. The axial points (red squares) are located along each axis at a given distance $\bar{a}$ from the centre point. In this work, $|\bar{a}| = 1$, so the axial points lie at the centre of the boundaries of the sampling domain, resulting in a face-centred CCD.

The CCD provides good coverage of the domain of interest and an efficient sampling scheme for fitting a second-order polynomial model. This formulation allows the relationships between inputs and outputs to be captured while also accounting for the curvature of the response surface. For instance, the number of samples is $2^d + 2d + 1$. In this case, with $d = 10$, the CCD generates $N_{\text{CCD}} = 1{,}045$ samples.

The CCD sampling is enriched with additional points generated using a full factorial design (FF).

Table 2 Summary of the selected inputs for the surrogate model, their statistical distributions, and their ranges of variation [20].

Parameter		Symbol [Unit]	Statistical distribution			Levels				
			Type	Nominal value (COV)	Coverage (%)	-1	$-\ell$	0	$+\ell$	+1
Friction coefficient		μ [-]	Normal	0.86 (8.5%)	99%	0.70	0.84	0.88	0.90	1.05
Vertical load		W [N]	Uniform	12,500 – 68,250 (-)	-	12,500	35,447	40,375	45,303	68,250
Thickness	Surface	h_1 [mm]	Normal	80 (12.5%)	99%	55	76	80	84	105
	Base	h_2 [mm]	Normal	260 (9.6%)	99%	195	249	260	271	325
Modulus	Surface	E_1 [MPa]	Lognormal	5,400 (20.0%)	95%	3,592	5,327	5,699	6,071	7,806
	Base	E_2 [MPa]	Lognormal	12,000 (20.0%)	95%	7,941	11,776	12,600	13,424	17,259
	Subgrade	E_3 [MPa]	Lognormal	95 (14.8%)	95%	70	93	98	102	125
Poisson's ratio	Surface	ν_1 [-]	Uniform	0.30 – 0.40 (-)	-	0.30	0.34	0.35	0.36	0.40
	Base	ν_2 [-]	Uniform	0.30 – 0.40 (-)	-	0.30	0.34	0.35	0.36	0.40
	Subgrade	ν_3 [-]	Uniform	0.30 – 0.45 (-)	-	0.30	0.36	0.38	0.39	0.45

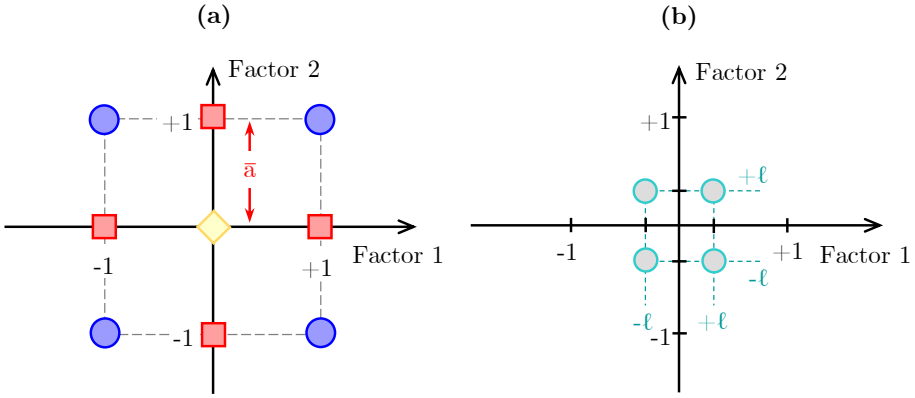

Fig. 4 Theoretical example of sampling designs obtained with two input factors using (a) a central composite design and (b) a full factorial design with levels set to $\pm\ell$, where $\ell < 1$.

The additional points are introduced for two reasons. First, they allow the polynomial degree to be customized for selected features when necessary, for example, to correct anomalous behaviour. Second, they increase the sampling density around the centre of the parameter space and provide additional coverage in this region. Their levels are set to $\pm\ell$, where $\ell = 2^{-d/4} \approx 0.18$ for $d = 10$. This choice is inspired by the conventional rotatable CCD, for which the prediction variance is distributed according to the distance from the centre of the design. The inner factorial levels are obtained by rescaling the conventional rotatable design so that its axial points coincide with the boundaries ± 1 of the present parameter space.

The supplementary FF design adds $N_{\mathrm{FF}} = 2^d = 1{,}024$ samples. The complete set of sampled points cannot be easily visualized graphically; therefore, Figure 4b shows a theoretical example of the additional FF samples for a two-dimensional parameter space.

The numerical experiment combining the CCD and FF designs therefore requires a total of 2,069 sampled parameter combinations, each corresponding to one calculation using the SAM. The CCD samples are exclusively retained for training. The FF samples are used either to train or to validate the surrogate model within the five-fold cross-validation procedure described in Section 3.4.

3.3 Mathematical formulation

The surrogate model is a polynomial response surface used as a transfer function to approximate the response of the semi-analytical model for a given set of input variables. The response surface is fitted independently at each mesh element, allowing the surrogate model to be expressed in matrix

form as:

$$\tilde{\mathbf{y}} = \mathbf{B}\boldsymbol{\Phi} + \boldsymbol{\epsilon} \tag{7}$$

where:

- $\tilde{\mathbf{y}} \in \mathbb{R}^{\kappa \times 1}$ is the vector of model responses, $\tilde{\mathbf{y}} = [\tilde{\mathrm{y}}_1 \tilde{\mathrm{y}}_2 \ldots \tilde{\mathrm{y}}_\kappa]^T$, with κ denoting the total number of mesh elements;
- $\boldsymbol{\Phi} \in \mathbb{R}^{\eta \times 1}$ is the vector of polynomial basis functions, $\boldsymbol{\Phi} = [\phi_1 \ \phi_2 \ \ldots \ \phi_\eta]^T$;
- $\mathbf{B} \in \mathbb{R}^{\kappa \times \eta}$ is the matrix of regression coefficients;
- $\boldsymbol{\epsilon} \in \mathbb{R}^{\kappa \times 1}$ is the vector of model errors, $\boldsymbol{\epsilon} = [\epsilon_1 \ \epsilon_2 \ \ldots \ \epsilon_\kappa]^T$.

The input vector is denoted $\tilde{\mathbf{x}} = [\tilde{\mathrm{x}}_1 \tilde{\mathrm{x}}_2 \ldots \tilde{\mathrm{x}}_d]^T$. It is standardised component-wise as:

$$\tilde{\mathbf{x}} = (\mathbf{x} - \bar{\mathbf{x}}) \oslash \boldsymbol{s}_{\mathbf{x}} \tag{8}$$

where $\oslash$ denotes element-wise division, $\mathbf{x} \in \mathbb{R}^{d \times 1}$ is the vector of original input variables, and $\bar{\mathbf{x}}$ and $\boldsymbol{s}_{\mathbf{x}}$ are the corresponding vectors of sample means and standard deviations, respectively, computed from the training set.

Each element of the polynomial basis $\boldsymbol{\Phi}$ is a monomial constructed from the components of $\tilde{\mathbf{x}}$. The set of retained monomials is defined as:

$$\begin{aligned} \mathcal{T} = \{1\} &\cup \{\tilde{\mathrm{x}}_m^p \mid 1 \le m \le d, 1 \le p \le \chi_m\} \\ &\cup \{\tilde{\mathrm{x}}_m \tilde{\mathrm{x}}_l \mid 1 \le m < l \le d\} \end{aligned} \tag{9}$$

where χ_m is the maximum polynomial degree considered for the standardised input $\tilde{\mathrm{x}}_m$, with the index $m \in \{1, 2, \ldots, d\}$. Following the sparsity principle, which assumes that low-order effects and interactions are more likely to be statistically significant [35], only first-order two-factor interactions are retained.

Based on these assumptions, the vector $\boldsymbol{\Phi}$ is defined as:

$$\begin{aligned} \boldsymbol{\Phi}(\tilde{\mathbf{x}}) = \Big[& 1, \tilde{\mathrm{x}}_1, \tilde{\mathrm{x}}_1^2, \ldots, \tilde{\mathrm{x}}_1^{\chi_1}, \\ & \tilde{\mathrm{x}}_2, \tilde{\mathrm{x}}_2^2, \ldots, \tilde{\mathrm{x}}_2^{\chi_2}, \ldots, \\ & \tilde{\mathrm{x}}_d, \tilde{\mathrm{x}}_d^2, \ldots, \tilde{\mathrm{x}}_d^{\chi_d}, \\ & \tilde{\mathrm{x}}_1 \tilde{\mathrm{x}}_2, \tilde{\mathrm{x}}_1 \tilde{\mathrm{x}}_3, \ldots, \tilde{\mathrm{x}}_{d-1} \tilde{\mathrm{x}}_d \Big]^T \end{aligned} \tag{10}$$

The number of monomials η depends on the number of input variables d and the maximum polynomial degree χ_m associated with each variable:

$$\eta = 1 + \sum_{m=1}^{d} \chi_m + \frac{d(d-1)}{2} \tag{11}$$

In the present study, a second-order polynomial is used for all input variables, except for the vertical load, for which a third-order term is introduced. The quadratic formulation led to anomalous behaviour for this variable, which was corrected by increasing its maximum polynomial degree to three. With $d = 10$, this results in $\eta = 67$ monomials.

The regression coefficients in $\mathbf{B}$ are estimated independently for each mesh element using ordinary least squares (OLS), by fitting the polynomial response surface to the samples of the training set (N_{train}). The corresponding design matrix $\tilde{\mathbf{X}} \in \mathbb{R}^{N_{\text{train}} \times \eta}$ is constructed by evaluating the polynomial basis $\boldsymbol{\Phi}$ at each standardised input vector in the training set. This procedure results in one set of regression coefficients for each mesh element.

Once the regression coefficients have been estimated, the surrogate model can be used to predict the response for unseen input parameters. Since the surrogate predictions are expressed in standardised units, they are converted back to the original physical scale (microstrains in the present study) according to:

$$\hat{\mathbf{y}} = \tilde{\mathbf{y}} \odot \boldsymbol{s}_{\mathbf{y}} + \bar{\mathbf{y}} \tag{12}$$

where:

- $\hat{\mathbf{y}} = [\hat{\mathrm{y}}_1 \ \hat{\mathrm{y}}_2 \ \ldots \ \hat{\mathrm{y}}_\kappa]^T$ is the vector of surrogate predictions in the original physical units;
- $\bar{\mathbf{y}} = [\bar{\mathrm{y}}_1 \ \bar{\mathrm{y}}_2 \ \ldots \ \bar{\mathrm{y}}_\kappa]^T$ is the vector of response means, with one value for each mesh element;
- $\boldsymbol{s}_{\mathbf{y}} = [\mathrm{SD}(\mathrm{y}_1) \ \mathrm{SD}(\mathrm{y}_2) \ \ldots \ \mathrm{SD}(\mathrm{y}_\kappa)]^T$ is the vector of response standard deviations calculated independently for each mesh element;
- $\odot$ denotes the element-wise product.

The means and standard deviations used for this transformation are calculated exclusively from the training set.

3.4 Training and testing process

The robustness of the surrogate model is assessed through a five-fold cross-validation procedure. In this work, the standard procedure is adapted.

The CCD samples are systematically retained in the training set because they provide coverage of the prescribed design space, including its boundaries. The FF samples are divided into five mutually exclusive folds, $\{\mathcal{F}_1, \mathcal{F}_2, \ldots, \mathcal{F}_5\}$. This results in five distinct training–validation configurations, or splits. For each split, the surrogate model is trained using all CCD samples and four of the five FF folds, while the remaining fold is used for testing. The test fold is iteratively alternated across the five splits, allowing the model to be evaluated on different subsets of FF samples. The FF samples thus provide additional information on the surrogate-model behavior within the design domain.

Figure 5 illustrates the cross-validation procedure. This strategy leads to a training set of approximately $N_{\text{train}} \approx 1,864$ samples (blue boxes), while the validation set contains the remaining $N_{\text{val}} \approx 205$ samples (red boxes) at each split.

3.5 Surrogate model-based analysis

Once validated, the surrogate model is employed to assess the influence of the input parameters on the pavement response and to characterize both expected spatial fields and localized critical responses. The analysis comprises two complementary steps: sensitivity analysis and uncertainty propagation.

3.5.1 Sensitivity analysis

Since the surrogate model is constructed as a polynomial response surface, derivative-based global sensitivity measures (DGSM) can be derived analytically directly from the regression coefficients. This framework provides a direct measure of how variations in an input feature affect the strain response field and allows for a ranking of feature influence.

The spatial sensitivity vector $\boldsymbol{\tau}_m \in \mathbb{R}^{\kappa \times 1}$ over the κ mesh elements is defined as the expectation of the squared partial derivative of the response vector $\tilde{\mathbf{y}}(\tilde{\mathbf{x}})$ with respect to $\tilde{\mathrm{x}}_m$, a given standardised feature with $m \in \{1, 2, \ldots, d\}$:

$$\boldsymbol{\tau}_m = \mathbb{E}\left[\left(\frac{\partial \tilde{\mathbf{y}}(\tilde{\mathbf{x}})}{\partial \tilde{\mathrm{x}}_m}\right)^2\right] = \int_{\Omega} \left(\frac{\partial \tilde{\mathbf{y}}(\tilde{\mathbf{x}})}{\partial \tilde{\mathrm{x}}_m}\right)^2 f(\tilde{\mathbf{x}})\, \mathrm{d}\tilde{\mathbf{x}} \tag{13}$$

where $f(\tilde{\mathbf{x}})$ denotes the joint probability density function of the standardised input parameters defined over the domain Ω. The square operation is applied element-wise over the spatial vector.

Using the matrix formulation of the surrogate model given in Equation 7, the partial derivative of the strain response vector with respect to the m-th feature is given by:

$$\frac{\partial \tilde{\mathbf{y}}(\tilde{\mathbf{x}})}{\partial \tilde{\mathrm{x}}_m} = \mathbf{B}\, \boldsymbol{\Phi}'_{,m}(\tilde{\mathbf{x}}) \tag{14}$$

where $\boldsymbol{\Phi}'_{,m}(\tilde{\mathbf{x}}) = \frac{\partial \boldsymbol{\Phi}(\tilde{\mathbf{x}})}{\partial \tilde{\mathrm{x}}_m} \in \mathbb{R}^{\eta \times 1}$ represents the partial derivative of the basis vector.

The sensitivity index $\boldsymbol{\tau}_m$ quantifies the mean-square rate of change of the response induced by parameter $\tilde{\mathrm{x}}_m$ over the input domain. Sobol and Kucherenko [36] established that DGSM indices provide an upper bound to the total Sobol sensitivity indices, which link response variance directly to input variability. Consequently, this derivative-based approach is particularly effective for screening out unessential features.

Because the expectation in Equation 13 is computed over the joint distribution $f(\tilde{\mathbf{x}})$, the sensitivity index naturally incorporates the statistical variability of the input parameters (Table 2). In addition, it automatically accounts for high-order interaction terms embedded in the surrogate model.

3.5.2 Uncertainty propagation

In complement to the sensitivity analysis, the stochastic analysis is performed by sampling the input parameters according to the probability distributions defined in Table 2. Latin Hypercube Sampling (LHS) [37] is adopted to generate the input realizations. In LHS, the range of each input variable is divided into equiprobable intervals, with one sample drawn from each interval. These samples are subsequently combined across dimensions to construct the multidimensional sample set. This stratified sampling scheme provides a more uniform coverage of the parameter space than standard Monte Carlo sampling, making it well-suited for uncertainty propagation in multi-dimensional problems.

A total of $N_{\text{LHS}} = 10^6$ samples were generated to evaluate the full strain response field. This sample size ensures pointwise convergence

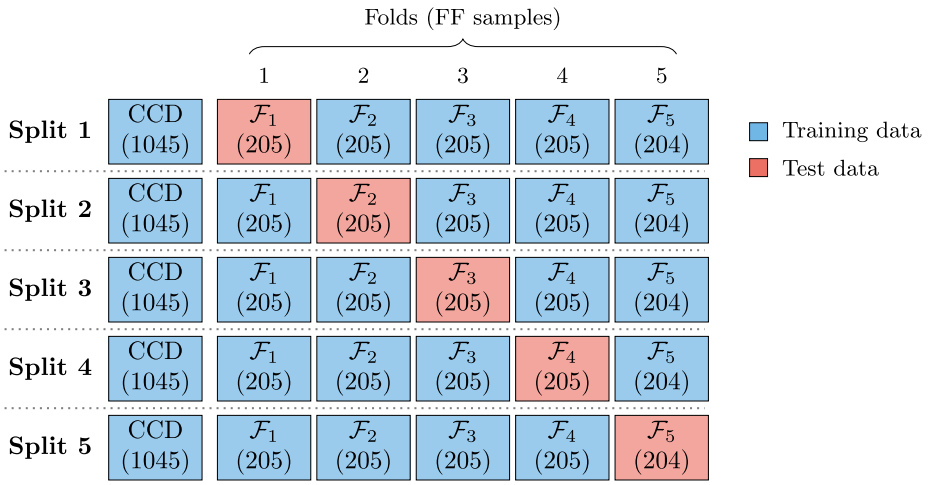

Fig. 5 Schematic representation of the distribution of samples between the training and validation sets during surrogate-model development. The number of samples is indicated in parentheses. Each split corresponds to a training–validation step and provides a separate performance assessment.

across the entire spatial domain, providing high-precision estimates for both central tendencies (median field) and upper-tail metrics (95th-percentile field).

4 Results and discussion

The contributions of this study are structured around three key aspects evaluated in this section: (i) the overall predictive accuracy and robustness of the surrogate model across the domain of interest; (ii) its application to global sensitivity analysis and the identification of spatial sensitivity patterns under severe braking; and (iii) the evaluation of critical strain responses, through uncertainty propagation, and their governing parameter ranges.

4.1 Surrogate model accuracy

The model is evaluated at each split using two conventional performance metrics, namely the coefficient of determination (R^2) and the root mean square error (RMSE). Since the surrogate model is fitted independently at each mesh element, these metrics are computed for each mesh element and each split. The geometry discretisation presented in Section 2.2.2 results in $\kappa = 13{,}335$ mesh elements on the pavement surface. Consequently, R^2 and RMSE are analyzed as distributions over the meshed surface. The goodness of fit is further illustrated at selected points on the pavement surface.

Figure 6 shows the distribution of the coefficient of determination over the meshed surface for each split, computed separately for the training and test sets.

The training sets show consistently high R^2 values, with a mean of 0.98, and 95% of the mesh elements over the pavement surface achieving $R^2 > 0.92$. The performance is slightly lower for the test sets, with a mean R^2 of 0.96. This is expected, as the metric is computed on samples that were not used to fit the surrogate model. The test sets also show a wider distribution of R^2 values across the mesh elements. In particular, the test fold of the fifth split exhibits the largest spread. Nevertheless, its fifth percentile is 0.83, meaning that 95% of the mesh elements still achieve an R^2 above this value. These results indicate good overall predictive performance of the surrogate model.

Figure 7 shows the RMSE distributions across the mesh elements for the five test folds, $\mathcal{F}_1$ to $\mathcal{F}_5$. The RMSE is computed from the standardised output and can therefore be interpreted in terms of the standard deviation of the local equivalent strain, normalised by its local mean. The similar shape of the histograms indicates consistent predictive performance across the five test folds. The RMSE values are generally small, with the

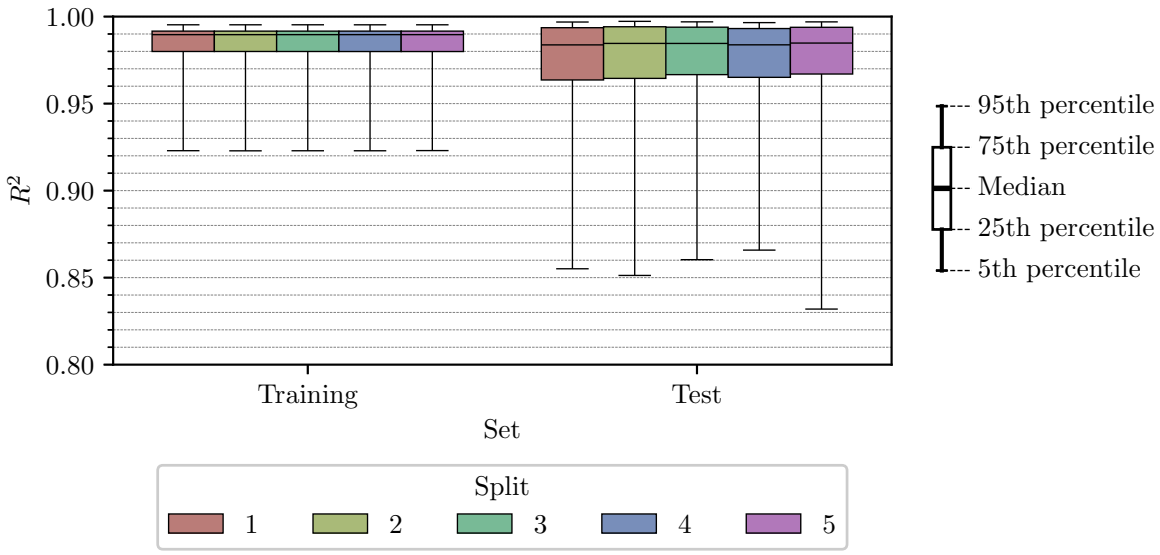

Fig. 6 Boxplots of R^2 values per mesh element for training and validation sets across cross-validation splits.

central 95% of the distributions ranging approximately from 0.009 to 0.060 standard deviations of the local equivalent strain. The distributions are concentrated towards lower RMSE values, with 75% of the mesh elements achieving an RMSE of 0.030 or less. The mean RMSE across the five test folds is approximately 0.026. These results indicate that, for the proposed sampling strategy, the surrogate model provides accurate predictions of the equivalent strain over most of the pavement surface within the prescribed parametric domain.

For further illustration of the local predictive behavior, Figure 8a compares the equivalent strain predicted by the surrogate model (y-axis) with the corresponding reference values obtained from SAM (x-axis). The axes are scaled such that the 1:1 diagonal line represents perfect agreement between the two models. The predicted values lie generally close to this line, indicating good agreement between the surrogate and the reference model at the selected surface locations (P_1 to P_4). The plots are constructed using out-of-sample test data (specifically fold $\mathcal{F}_4$), evaluating the surrogate at input parameter combinations unseen during training while remaining strictly within the interpolation domain.

Figure 8b complements this analysis by displaying the residual distributions at the same spatial locations. The prediction performance on test data was evaluated using standardised residuals, normalised by the residual variance estimated from the corresponding spatial node during training. The histograms of the standardised residuals are centered near zero and exhibit a distribution broadly consistent with normality, thus supporting the core assumptions of the ordinary least squares formulation. Furthermore, the standardised residuals remain tightly bounded within the interval $[-1, +1]$, demonstrating high predictive accuracy and an absence of extreme outliers at the evaluated points.

Figure 9 compares the equivalent strain fields predicted by the semi-analytical model (left) and the surrogate model (right) for two selected test samples, (a) and (b). The corresponding input parameters are reported in Table 3. The vertical load is identical for both samples, whereas sample (a) has lower stiffnesses in the surface and base layers and a thicker surface course. These parameters result in maximum strains of approximately 303 $\mu\varepsilon$ and 271 $\mu\varepsilon$ for samples (a) and (b), respectively. For both samples, the maximum strains occur beneath the rear part of each tyre tread, as expected under tractive loading conditions [14].

The predicted equivalent strain fields closely match the reference SAM fields for both test samples. The symmetry of the strain field with respect to the longitudinal axis is also preserved, with the response mirrored on either side of the axis. For

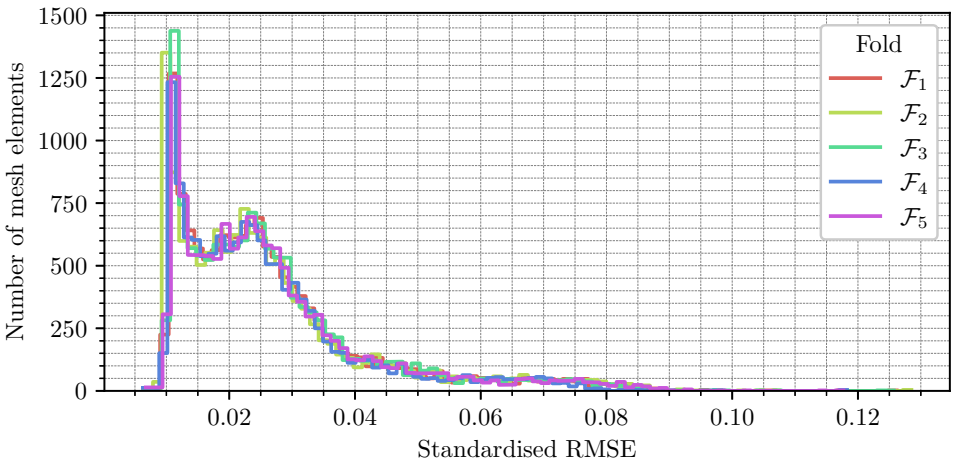

Fig. 7 Histograms of standardised RMSE per mesh element for each test fold $\{\mathcal{F}_1, \mathcal{F}_2, \ldots, \mathcal{F}_5\}$.

comparison, the relative error $\epsilon_{i,\mathrm{rel}}$ at each element i of the meshed pavement surface is computed with respect to the reference SAM prediction as:

$$\epsilon_{i,\mathrm{rel}}\,[\%] = \frac{\left|\hat{\varepsilon}^{(i)}_{\mathrm{surrogate}} - \hat{\varepsilon}^{(i)}_{\mathrm{SAM}}\right|}{\left|\hat{\varepsilon}^{(i)}_{\mathrm{SAM}}\right|} \times 100 \qquad (15)$$

where $\hat{\varepsilon}^{(i)}_{\mathrm{SAM}}$ and $\hat{\varepsilon}^{(i)}_{\mathrm{surrogate}}$ denote the reference SAM and surrogate-model predictions, respectively, at element $i \in \{1, 2, \ldots, \kappa\}$.

The maximum equivalent strains predicted by the surrogate model differ from the reference values by only 0.1% for sample (a) and 2.5% for sample (b). The mean element-wise relative errors between the predicted and reference fields are approximately 1.0% for sample (a) and 2.4% for sample (b), while the 99th-percentile relative errors remain below 6.7% and 9.3%, respectively. The largest local relative errors occur at locations where the strain levels are relatively modest, approximately 6 $\mu\varepsilon$ and 47 $\mu\varepsilon$ for samples (a) and (b), respectively. This indicates that the larger relative errors are concentrated in regions of low strain and therefore have a limited influence on the prediction of the critical strain levels.

The surrogate model also provides a substantial reduction in computational cost and memory requirements. Once the polynomial basis is constructed, surrogate evaluation reduces to a matrix–vector product of size $\kappa \times \eta$, where κ is the number of mesh elements and η is the number of polynomial monomials. Its computational cost therefore scales as $\mathcal{O}(\kappa\eta)$. For the present configuration, the basis matrix requires less than 10 MB of memory and a complete surrogate evaluation takes approximately 4 ms on a standard laptop computer, compared with several minutes for a single evaluation of the full semi-analytical model.

For the analyses presented in Section 4.2, the final surrogate model is refitted using all available samples ($N_{\mathrm{CCD}} + N_{\mathrm{FF}} = 2{,}069$). This refined model is subsequently employed to perform the sensitivity analysis and evaluate critical strain responses.

4.2 Sensitivity analysis

The surrogate model is used to identify the input parameters that most strongly influence the surface strain field. Sensitivity indices are evaluated both across the full spatial domain and at individual nodes to reveal their spatial distribution patterns.

4.2.1 Overall ranking of input parameters

Figure 10 presents boxplots of the relative sensitivity index $\boldsymbol{\tau}_{m,\mathrm{rel}} \in \mathbb{R}^{\kappa\times 1}$ across all mesh elements for each input parameter m, ranked in descending order according to their median value. For each node i, this index is defined as the sensitivity to parameter m normalised by the sum of sensitivities across all d input parameters, as formulated in Equation 16. This normalization facilitates a direct comparison of the global

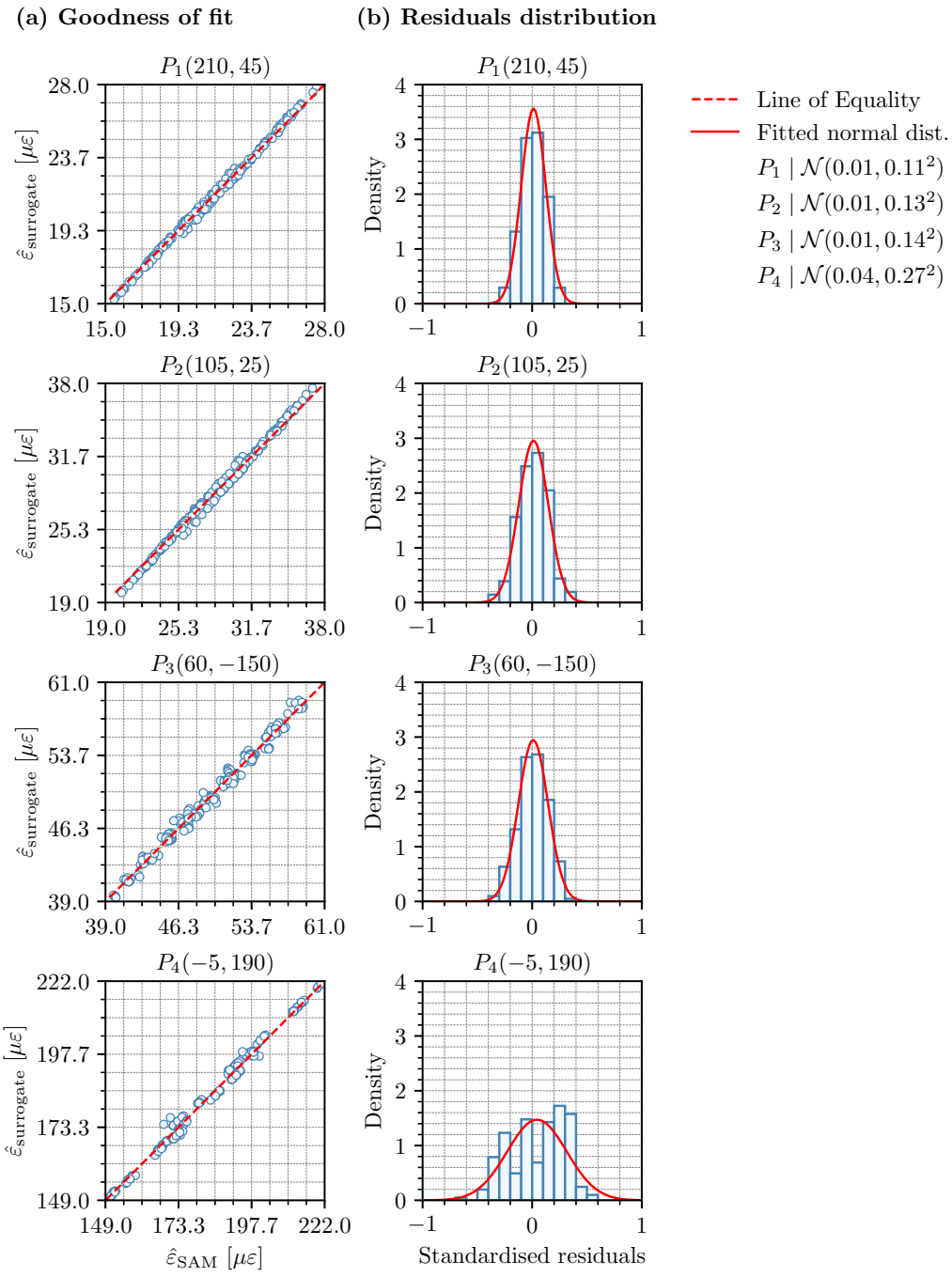

Fig. 8 Surrogate model local accuracy at four spatial locations $P_i(x_i, y_i)$, $i \in \{1, \ldots, 4\}$ (x, y: longitudinal and lateral coordinates): (a) predicted ($\hat{\varepsilon}_{\text{surrogate}}$) vs. expected ($\hat{\varepsilon}_{\text{SAM}}$) strain values, and (b) distribution of standardised residuals.

Table 3 Input parameter values for samples (a) and (b).

Samples	Inputs									
	μ	W [N]	E_1 [MPa]	ν_1	h_1 [mm]	E_2 [MPa]	ν_2	h_2 [mm]	E_3 [MPa]	ν_3
(a)	0.84	45,303	5,327	0.34	84	11,776	0.34	271	93	0.36
(b)	0.84	45,303	6,071	0.34	76	13,424	0.34	271	93	0.36

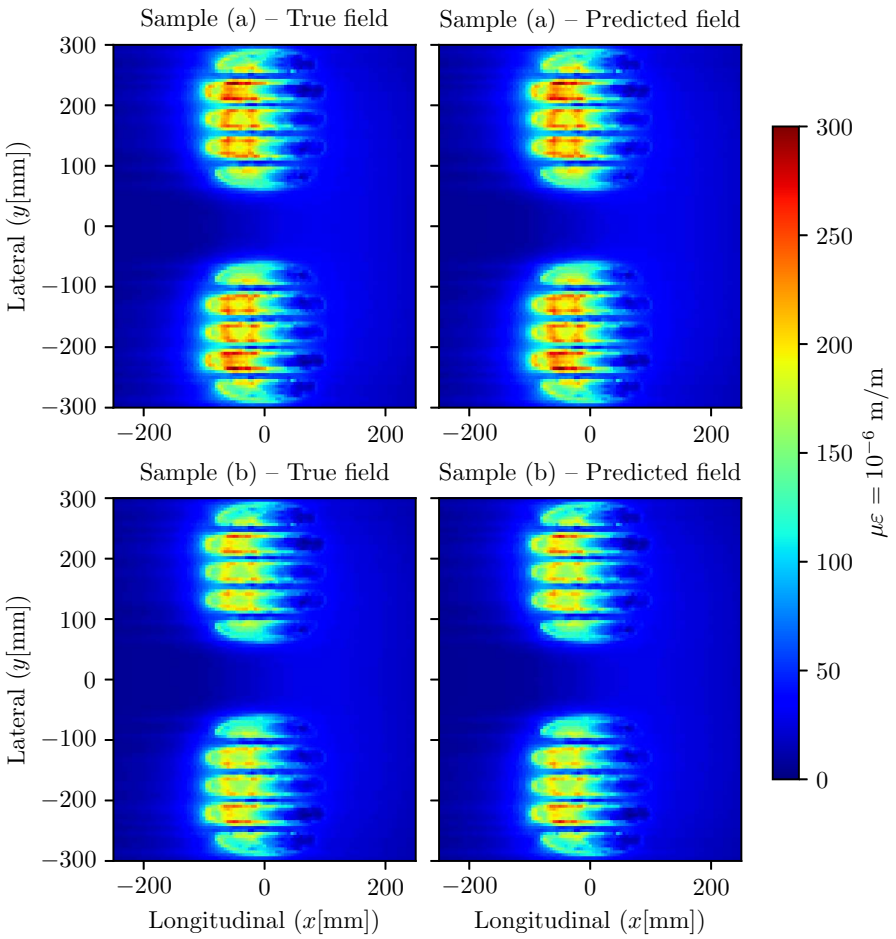

Fig. 9 Comparison between the reference and predicted strain fields at the pavement surface.

influence of each parameter across the pavement surface domain.

$$\tau_{m,\mathrm{rel}}^{(i)} = \frac{\tau_m^{(i)}}{\sum_{k=1}^{d} \tau_k^{(i)}}, \text{ with } \sum_{m=1}^{d} \tau_{m,\mathrm{rel}}^{(i)} = 1 \quad (16)$$

The results indicate that the vertical load (W) has a pronounced influence on the equivalent strain field at the tyre–pavement interface. It is followed, in decreasing order of median relative sensitivity, by the elastic modulus of the surface layer (E_1), the thickness of the base layer (h_2), the friction coefficient (μ), and the Poisson's ratio

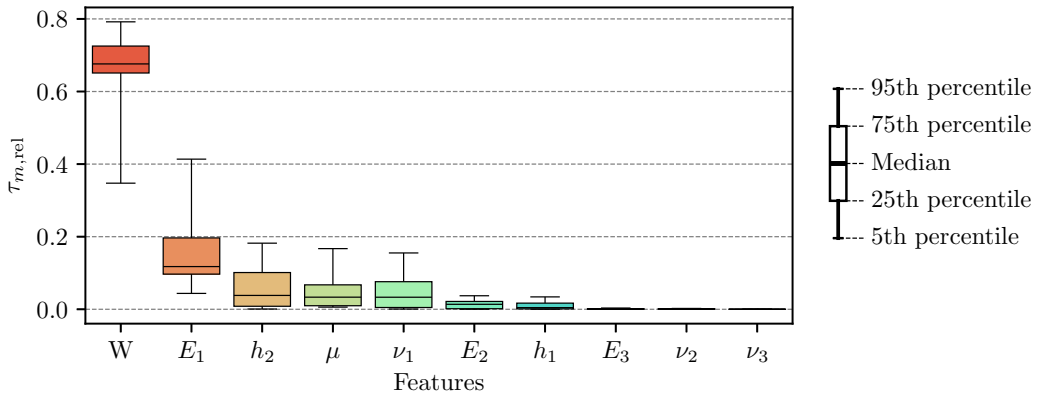

Fig. 10 Boxplots of the relative sensitivity index per mesh element for the selected input parameters.

of the surface layer (ν_1). In contrast, the mechanical properties of the adjacent layers (E_2 and ν_2 for the base layer, and E_3 and ν_3 for the subgrade layer), together with the thickness of the surface layer (h_1), exhibit substantially lower relative sensitivities across the meshed surface.

The relative sensitivity to the vertical load (W) ranges from 0.35 at the 5th percentile to 0.79 at the 95th percentile, with a median value of 0.68 across the mesh elements. The elastic modulus of the surface layer (E_1) also exhibits a relatively wide range, from 0.04 at the 5th percentile to 0.41 at the 95th percentile, although its influence is less pronounced than that of the vertical load.

The remaining influential features (h_2, μ and ν_1) exhibit comparable median relative sensitivity indices and similar ranges of variation. The friction coefficient (μ) and the Poisson's ratio (ν_1) of the surface course both have a median relative sensitivity index of approximately 0.03, reaching 0.17 and 0.16, respectively, at the 95th percentile. The base-layer thickness (h_2) exhibits a slightly higher median relative sensitivity index of 0.04 and reaches 0.18 at the 95th percentile.

These results are broadly consistent with the preliminary screening analysis conducted by the same authors [20]. However, they also highlight the influence of the base-layer thickness, which is found to be comparable to that of μ and ν_1. This additional finding can be attributed to the present analysis accounting simultaneously for the individual and coupled contributions of the surrogate-model terms, as well as for the statistical distributions assigned to the input parameters. It therefore provides a more comprehensive assessment of their influence over the prescribed parameter domain.

Overall, the analysis identifies the input features that have the greatest influence on the surface equivalent strain field. However, the ranking based on the global distribution of the sensitivity index does not capture its spatial variability. A more detailed assessment is therefore presented in Section 4.2.2, focusing on the distribution of sensitivity across the pavement surface and, in particular, on the regions where high surface strains are predicted.

4.2.2 Spatial analysis

Uncertainty propagation enabled the reconstruction of the probabilistic distribution of the equivalent strain field over the specified input domain of the surrogate model. Figure 11 illustrates the equivalent strain fields corresponding to the (a) 50th percentile, (b) 75th percentile, and (c) 95th percentile of the predicted response. These fields identify the regions of the pavement surface associated with the highest strain levels and, consequently, those potentially more susceptible to surface-initiated damage.

For comparison, the regions where the equivalent strain exceeds the adopted fatigue criterion, $\varepsilon_6 = 150\ \mu\varepsilon$, are delineated by a black line. This value corresponds to the approximate tensile strain level associated with fatigue cracking after 10^6 load cycles for the dense bituminous surface material considered in this study, based on fatigue testing conducted at 10 °C and 25 Hz. As the percentile level increases, the region exceeding this criterion progressively expands from the rear

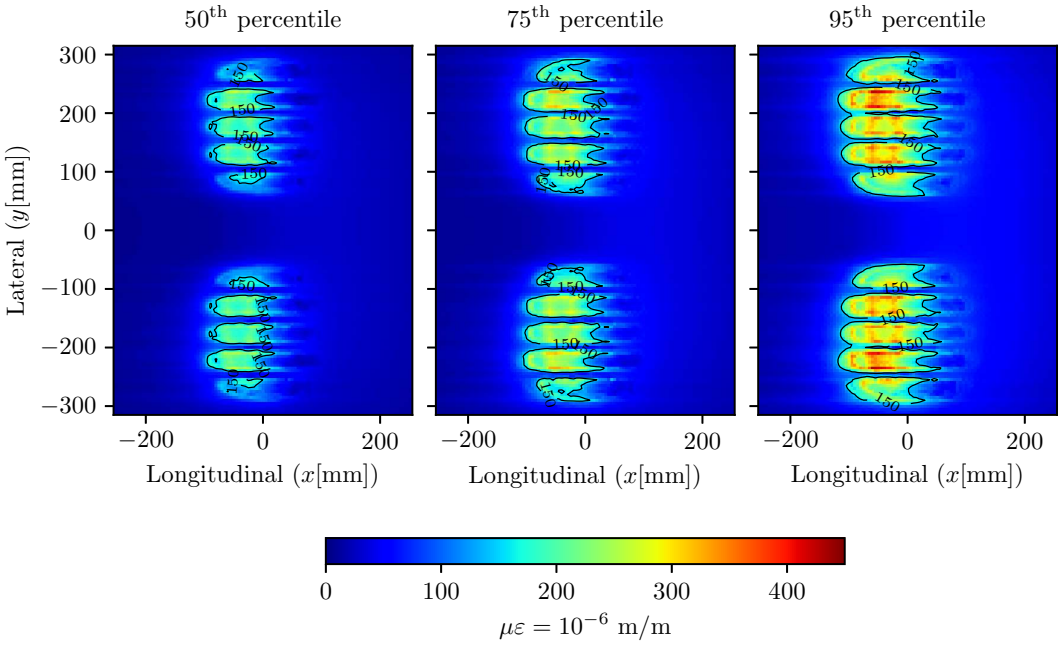

Fig. 11 Equivalent strain fields at selected percentiles of the predicted response: (a) 50th percentile, (b) 75th percentile, and (c) 95th percentile.

towards the front of the tyre–pavement interaction zone.

The maximum strain levels are substantially higher than ε_6, increasing from approximately 271 $\mu\varepsilon$ for the median strain field (Figure 11a) to 427 $\mu\varepsilon$ for the 95th-percentile strain field (Figure 11c). This indicates that the considered flexible pavement structure is prone to severe surface tensile strains when subjected to adverse combinations of severe tractive loading and parametric variability.

Figure 12 shows the spatial distribution of the relative sensitivity index $\tau_{m,\mathrm{rel}}$ for the five parameters identified as the most influential (cf. Section 4.2): (a) vertical load (W), (b) surface-course modulus (E_1), (c) base-course thickness (h_2), (d) friction coefficient (μ), and (e) surface-course Poisson's ratio (ν_1). A distinct tyre-shaped pattern is observed in the sensitivity fields, indicating that the underlying tyre–pavement contact geometry strongly influences the local sensitivity of the model. This pattern is consistent with the equivalent strain distributions shown in Figure 11 and is hereafter referred to as the *contact-dominated zone*.

The vertical load, surface-course modulus, and friction coefficient exhibit the greatest sensitivity within regions associated with peak strain levels, which are concentrated towards the rear of the contact-dominated zones.

Figure 12a confirms the overall predominance of the vertical load (W) across the pavement surface. The vertical load remains influential outside the contact-dominated zones, where tensile strains are predominantly associated with global pavement bending. Because the braking force depends directly on the vertical load (Section 2.2.4), variations in W alter the overall stress state – including tangential tractions – leading to high sensitivity near the trailing edges of the contact areas.

In contrast, the influence of the surface-course modulus (E_1) becomes more pronounced towards the central regions of the contact-dominated zone, as shown in Figure 12b. A similar spatial concentration is observed for the friction coefficient (μ) in Figure 12d.

Moreover, the pronounced sensitivity to the friction coefficient within the contact-dominated zone further highlights the importance of explicitly accounting for tyre–pavement interaction when predicting surface tensile strains. Because

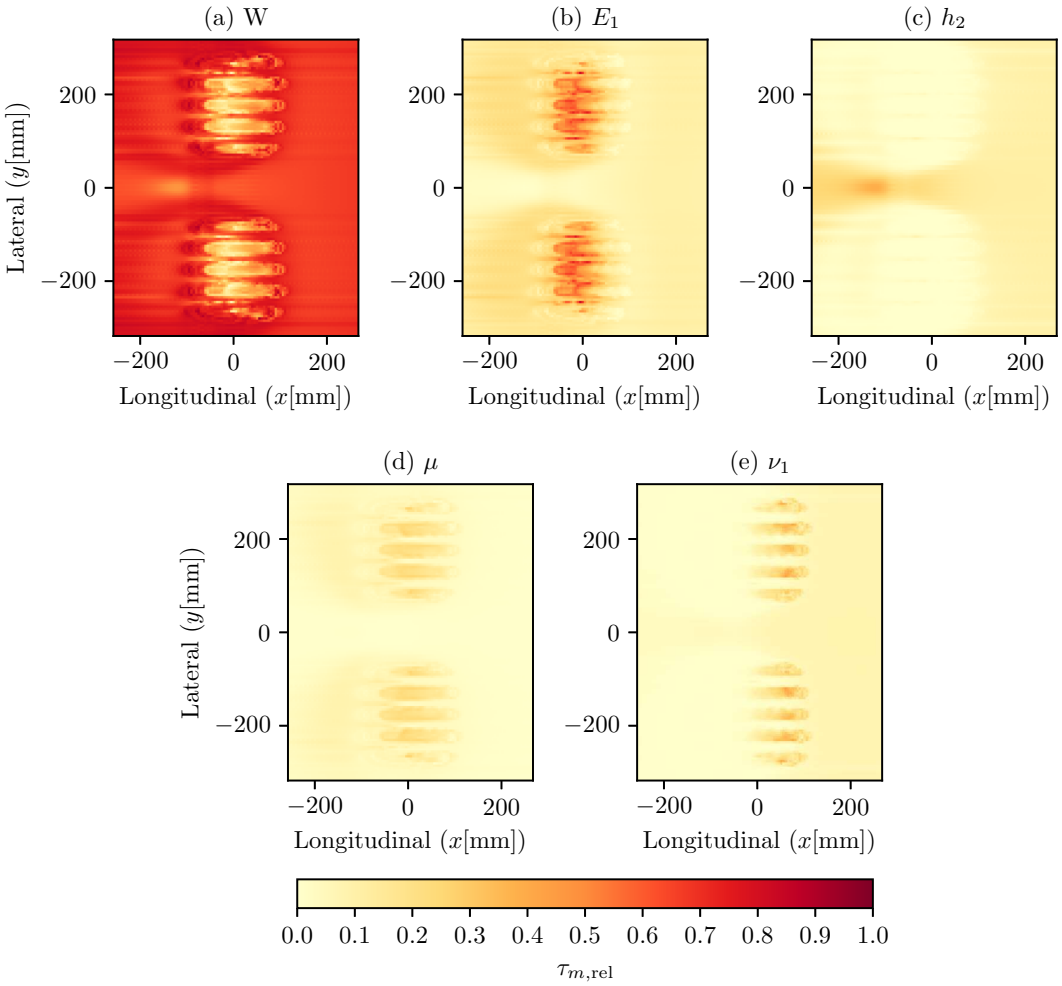

Fig. 12 Spatial distribution of the relative sensitivity index for the selected input parameters: (a) vertical load (W), (b) surface-course modulus (E_1), (c) base-course thickness (h_2), (d) friction coefficient (μ), and (e) Poisson's ratio of the surface course (ν_1).

μ directly governs the magnitude of tangential stresses under braking, its effect is particularly dominant where the strain response is driven by tractive loading.

Although base-course thickness (h_2), friction coefficient (μ), and surface-course Poisson's ratio (ν_1) exhibit comparable median sensitivity over the pavement surface, their spatial distributions differ significantly. Sensitivity to h_2 is more pronounced in the region between the two tyre footprints, whereas ν_1 exerts a greater influence near the upper-front region of the footprints. These distinct spatial distributions demonstrate that parameters with similar overall sensitivity metrics can govern entirely different critical regions on the pavement surface.

4.3 Stochastic analysis of critical responses

The critical response for surface damage is defined as the spatial maximum equivalent strain:

$$\hat{\varepsilon}_{\max}(\tilde{\mathbf{X}}) = \max_{i\in\{1,\ldots,\kappa\}} \hat{\varepsilon}_i(\tilde{\mathbf{X}}) \tag{17}$$

where κ denotes the total number of mesh elements on the pavement surface. Uncertainty propagation yields the maximum equivalent strain

across the ensemble of random input realizations, denoted by $\tilde{\mathbf{X}} = \{\tilde{\mathbf{x}}_1, \tilde{\mathbf{x}}_2, \ldots, \tilde{\mathbf{x}}_{N_{\text{LHS}}}\}$.

Figure 13 presents the empirical distribution of the maximum equivalent strain evaluated across a sample size of $N_{\text{LHS}} = 10^6$. The histogram exhibits a slightly right-skewed profile, characterized by a higher probability density in the lower range and an elongated upper tail. The candidate theoretical distributions yielding the closest fit are the Beta, Gamma, and Lognormal distributions, determined by minimizing the sum of squared errors (SSE) between the empirical and theoretical cumulative distribution functions. Accordingly, the median critical strain is 283 $\mu\varepsilon$; however, owing to the positive skewness, the critical strain reaches 340 $\mu\varepsilon$ at the 75th percentile and 432 $\mu\varepsilon$ at the 95th percentile. A slight discrepancy is observed when compared to the maximum strain levels extracted from the statistical response fields (Figure 11) because the spatial location of the peak strain shifts across parameter realizations, which causes node-by-node statistical estimates to underestimate sample-wise spatial maxima.

To identify the input parameter combinations associated with distinct severity levels of the critical strain, the input domain Ω is partitioned according to the quantiles of the empirical response distribution. A response-conditioned subset of the input domain is defined as:

$$\mathcal{D}_{[\theta_1,\theta_2)} = \left\{ \tilde{\mathbf{x}} \in \Omega : F^{-1}(\theta_1) \leq \hat{\varepsilon}_{\max}(\tilde{\mathbf{x}}) < F^{-1}(\theta_2) \right\}, \quad 0 \leq \theta_1 < \theta_2 \leq 1 \tag{18}$$

where F denotes the empirical cumulative distribution function of the maximum equivalent strain, and θ_1, θ_2 represent the lower and upper quantile thresholds, respectively.

Four specific subdomains are examined: (a) $\mathcal{D}_{<0.50}$, (b) $\mathcal{D}_{[0.50,0.75)}$, (c) $\mathcal{D}_{[0.75,0.95)}$, and (d) $\mathcal{D}_{\geq 0.95}$, which correspond to the lower 50%, 50–75%, 75–95%, and upper 5% quantile ranges of the empirical response distribution, respectively. The conditional distribution of each input parameter within these selected subdomains is illustrated in Figure 14. To maintain continuity, the parameters are ordered according to the same descending relative-sensitivity ranking established in the previous analyses. For readability, the input magnitudes are presented in dimensionless coded form, with the vertical axes corresponding to the parameter levels defined in the DoE framework (Section 3.2).

These results reveal distinct patterns in the response-conditioned input distributions. Notably, input parameters identified as less influential with respect to the surface equivalent strain field exhibit near-identical distributions across all subdomains. This behavior is observed for the mechanical properties of the base layer (E_2, ν_2) and subgrade (E_3, ν_3), as well as the thickness (h_1) of the surface layer. Furthermore, although the base-layer thickness (h_2) exhibits moderate sensitivity across the broader strain field, its conditional distribution remains virtually unchanged across the response subdomains, indicating a limited influence on high strain levels.

In contrast, the input parameters identified as most influential for the critical surface strain display distinct shifts in their conditional distributions with increasing response severity.

The most marked shift is observed for the vertical load (W). For maximum strain levels below the median ($\mathcal{D}_{<0.50}$, Figure 14a), W exhibits a higher probability density toward its lower coded values, with a conditional median of -0.44. Its distribution shifts toward higher coded values, attaining a conditional median of $+0.18$ in the 50–75% response subdomain ($\mathcal{D}_{[0.50,0.75)}$, Figure 14b) and $+0.51$ in the 75–95% response subdomain ($\mathcal{D}_{[0.75,0.95)}$, Figure 14c). This shift becomes particularly pronounced in the 5% upper response subdomain ($\mathcal{D}_{\geq 0.95}$, Figure 14d), where approximately 75% of the conditional distribution of W lies above $+0.60$, with its conditional median reaching $+0.79$.

The friction coefficient (μ) and surface-course Poisson's ratio (ν_1) exhibit a similar, albeit substantially weaker, trend. For the lower 50% of maximum strain responses ($\mathcal{D}_{<0.50}$, Figure 14a), their conditional medians are -0.18 and -0.08, respectively. In the 50–75% response subdomain ($\mathcal{D}_{[0.50,0.75)}$, Figure 14b), the corresponding medians move toward the center of the coded range, reaching -0.04 and $+0.03$. In the 5% upper response subdomain ($\mathcal{D}_{\geq 0.95}$, Figure 14d), the medians attain $+0.21$ and $+0.23$, respectively, a comparatively modest shift toward higher coded values.

An inverse behaviour is observed for the surface-course elastic modulus (E_1), where

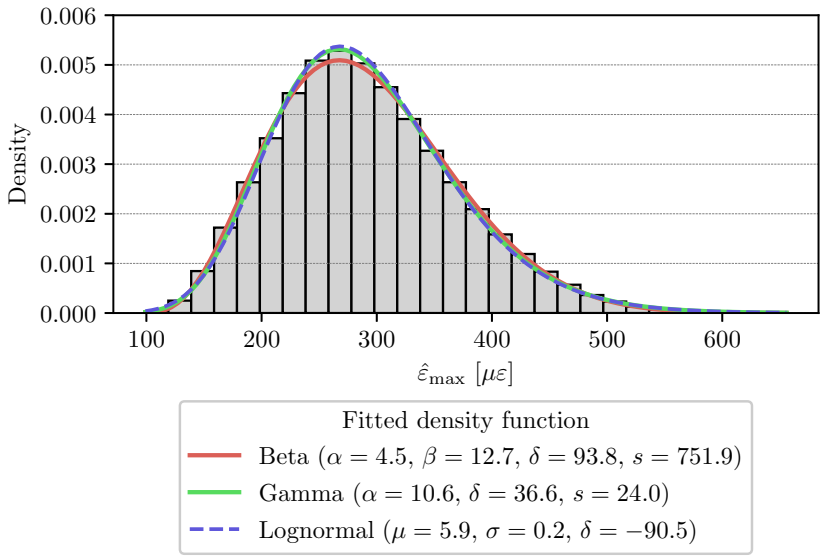

Fig. 13 Histogram of the maximum equivalent strain ($N_{\text{LHS}} = 10^6$). Fitted parameters are summarized for each density function, with δ the shift parameter and s the scale parameter.

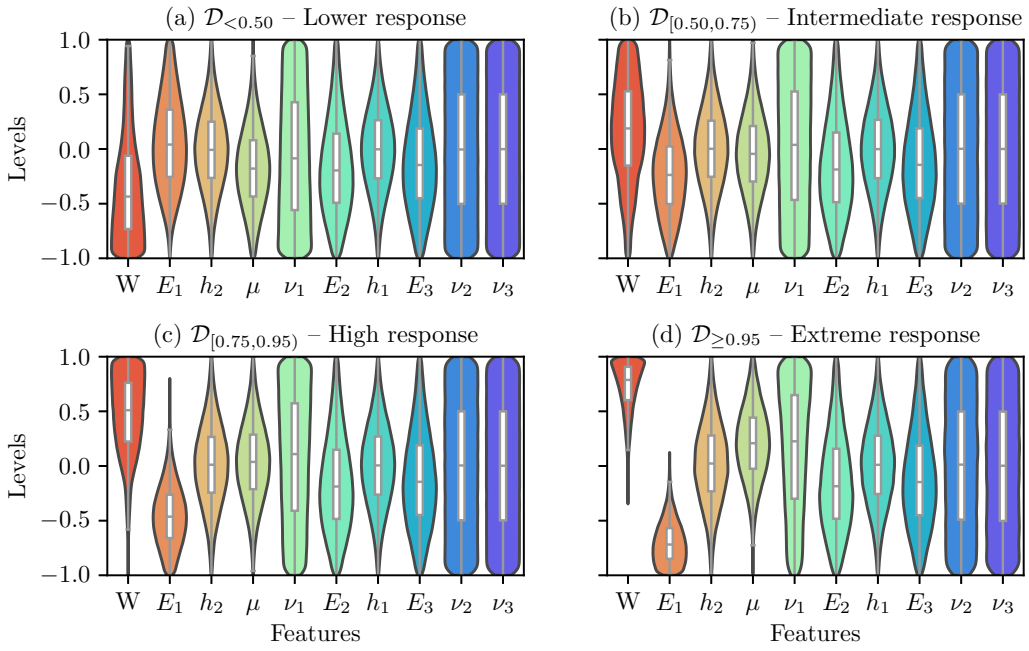

Fig. 14 Conditional distributions of the input parameters for different levels of maximum equivalent strain: (a) lower 50% of responses, (b) 50–75% of responses, (c) 75–95% of responses, and (d) upper 5% of responses.

increasingly critical strains correlate with systematically lower modulus values. Its conditional median shifts from +0.04 in $\mathcal{D}_{<0.50}$ (Figure 14a) to −0.24 in $\mathcal{D}_{[0.50,0.75)}$ (Figure 14b), reaching −0.72 in the 5% upper subdomain ($\mathcal{D}_{\geq 0.95}$, Figure 14d). Specifically, for these critical strain levels, 75% of the conditional E_1 distribution falls

below -0.57. This behaviour directly opposes that of the vertical load (W).

Overall, these results indicate that severe strains levels are primarily associated with high vertical loads (W) and low surface-course moduli (E_1), with moderate contributions from higher friction coefficients (μ) and Poisson's ratios (ν_1). Conversely, the conditional distributions of the layer thicknesses and underlying layer properties remain largely unchanged relative to their marginal distributions for critical responses.

These findings highlight two parameters frequently simplified or omitted in standard pavement design: the surface-course Poisson's ratio, which is typically assumed rather than measured, and the friction coefficient, which is generally ignored in conventional models that simplify tyre–pavement interaction.

5 Conclusions

Accurate and efficient prediction of pavement stress and strain fields is important for improving pavement design and maintenance strategies. For surface distress phenomena under critical vehicle manoeuvres, realistic tyre–pavement contact cannot be neglected. This study addressed two main aspects: the development of computationally efficient numerical and mathematical tools for tyre–pavement interaction, and their use to quantify uncertainty, identify critical responses, and assess the influence of input parameters. A single case study was considered, with linear elastic constitutive behaviour and input parameters commonly used in pavement design. The main findings are summarised as follows:

- A matrix-form polynomial surrogate model provides an efficient tool for large-scale analysis, accurately reproducing the equivalent surface strain response while reducing the computational cost by several orders of magnitude (at least 75,000 times). This efficiency enables stochastic analyses that would otherwise be impractical with computationally intensive contact models.
- The critical surface strain response is governed predominantly by the vertical load and the stiffness of the surface course. The friction coefficient and surface-course Poisson's ratio also contribute to the response, particularly within the contact-dominated region. These findings highlight the importance of considering both loading and near-surface material properties when assessing pavement response under tractive loading.
- The combination of surrogate modelling and probabilistic analysis provides a practical framework for identifying the input ranges associated with critical pavement responses. In the present case, high responses are primarily associated with high vertical loads and low surface-course stiffness, while the conditional distributions of the remaining layer properties remain largely unchanged. The approach therefore enables the identification of combinations of uncertain parameters associated with critical responses, rather than merely quantifying response variability.

The proposed framework can be extended to other loading conditions and pavement structures. The computational efficiency of the reference semi-analytical model facilitates the extension of the database and the generation of additional samples for new scenarios. The developed response surface also provides a simple and interpretable approach for surrogate modelling of spatial fields. Further improvements could focus on increasing sampling efficiency through adaptive sampling strategies and on reducing the dimensionality of the surrogate model. Future work should also consider more complex scenarios with nonlinear and time-dependent material behaviour.

Declarations

Authorship contribution statement. D. C. S. developed the methodology, conducted the formal analysis and investigation, and prepared the original manuscript. N. R. R., S. Y., and B. P. contributed to the conceptualisation of the study, reviewed and edited the manuscript, and supervised the work. P. R. and C. P. contributed to the conceptualisation and supervision of the study.

Competing Interests. The authors have no competing interests to declare that are relevant to the content of this article.

Data availability. The authors declare that the data supporting the findings of this study are presented within the paper. The underlying raw data are not publicly available. Requests for access

to specific datasets may be addressed to the corresponding author and will be considered on a case-by-case basis.

References

[1] Myers, L.A., Roque, R., Ruth, B.E., Drakos, C.: Measurement of Contact Stresses for Different Truck Tire Types To Evaluate Their Influence on Near-Surface Cracking and Rutting. Transportation Research Record: Journal of the Transportation Research Board **1655**(1), 175–184 (1999) https://doi.org/10.3141/1655-23

[2] De Beer, M., Fisher, C., Jooste, F.J.: Determination of pneumatic tyre/pavement interface contact stresses under moving loads and some effects on pavements with thin asphalt surfacing layers. In: Proceedings of the 8th International Conference on Asphalt Pavements, vol. 1, pp. 179–227. University of Washington, Seattle (1997)

[3] Wang, H., Al-Qadi, I.L.: Combined Effect of Moving Wheel Loading and Three-Dimensional Contact Stresses on Perpetual Pavement Responses. Transportation Research Record: Journal of the Transportation Research Board **2095**(1), 53–61 (2009) https://doi.org/10.3141/2095-06

[4] Hajj, E.Y., Thushanthan, P., Sebaaly, P.E., Siddharthan, R.V.: Influence of Tire–Pavement Stress Distribution, Shape, and Braking on Performance Predictions for Asphalt Pavement. Transportation Research Record: Journal of the Transportation Research Board **2306**(1), 73–85 (2012) https://doi.org/10.3141/2306-09

[5] Manyo, E.Y., Reynaud, P., Picoux, B., Tautou, R., Nelias, D., Allou, F., Petit, C.: Towards fast modelling of the tire-pavement contact. European Journal of Environmental and Civil Engineering **25**(13), 2396–2412 (2021) https://doi.org/10.1080/19648189.2019.1628812

[6] Wang, H., Al-Qadi, I.L.: Evaluation of Surface-Related Pavement Damage due to Tire Braking. Road Materials and Pavement Design **11**(1), 101–121 (2010) https://doi.org/10.1080/14680629.2010.9690262

[7] Hammoum, F., Chabot, A., St-Laurent, D., Chollet, H., Vulturescu, B.: Effects of accelerating and decelerating tramway loads on bituminous pavement. Materials and Structures **43**(9), 1257–1269 (2010) https://doi.org/10.1617/s11527-009-9577-9

[8] Wang, H., Al-Qadi, I.L., Stanciulescu, I.: Effect of Surface Friction on Tire–Pavement Contact Stresses during Vehicle Maneuvering. Journal of Engineering Mechanics **140**(4), 04014001 (2014) https://doi.org/10.1061/(ASCE)EM.1943-7889.0000691

[9] Király, T., Primusz, P., Tóth, C.: Simulation of Static Tyre–Pavement Interaction Using Two FE Models of Different Complexity. Applied Sciences **12**(5), 2388 (2022) https://doi.org/10.3390/app12052388

[10] Cardenas, J.J., Jayme, A., Hernandez, J., Al-Qadi, I.L.: Quantification of Truck Electrification Damage to Flexible Pavements. Transportation Research Record: Journal of the Transportation Research Board, 03611981261473504 (2026) https://doi.org/10.1177/03611981261473504

[11] Ge, H., Quezada, J.C., Le Houerou, V., Chazallon, C., Sha, A.: From macro to micro: Investigation of three-dimensional particle-scale responses of asphalt mixtures under non-uniform rolling tire loads via coupled FEM-DEM simulations. Road Materials and Pavement Design, 1–30 (2025) https://doi.org/10.1080/14680629.2025.2478617

[12] Liu, P., Wang, D., Oeser, M.: Application of semi-analytical finite element method coupled with infinite element for analysis of asphalt pavement structural response. Journal of Traffic and Transportation Engineering (English Edition) **2**(1), 48–58 (2015) https://doi.org/10.1016/j.jtte.2015.01.005

[13] Shen, K., Zhang, H., Tong, J., Wang, H., Chen, X.: Dynamic elastic analysis of flexible pavements under moving vehicles:

A semi-analytical finite element treatment. Road Materials and Pavement Design **23**(6), 1440–1450 (2022) https://doi.org/10.1080/14680629.2021.1883467

[14] Manyo, E.Y., Picoux, B., Reynaud, P., Tautou, R., Nelias, D., Allou, F., Petit, C.: Approach of Pavement Surface Layer Degradation Caused by Tire Contact Using Semi-Analytical Model. Materials **14**(9), 2117 (2021) https://doi.org/10.3390/ma14092117

[15] Ziyadi, M., Al-Qadi, I.L.: Efficient surrogate method for predicting pavement response to various tire configurations. Neural Computing and Applications **28**(6), 1355–1367 (2017) https://doi.org/10.1007/s00521-016-2442-1

[16] Liu, X., Jayme, A., Al-Qadi, I.L.: ContactGAN development – prediction of tire-pavement contact stresses using a generative and transfer learning model. International Journal of Pavement Engineering **24**(2), 1–11 (2022) https://doi.org/10.1080/10298436.2022.2138876

[17] Lang, H., Villamil, W.D., Al-Qadi, I.L.: 3D tire–pavement contact stresses: Physics-informed prediction approach. International Journal of Pavement Engineering **27**(1), 2621970 (2026) https://doi.org/10.1080/10298436.2026.2621970

[18] Okte, E., Al-Qadi, I.L.: Prediction of flexible pavement 3-D finite element responses using Bayesian neural networks. International Journal of Pavement Engineering **23**(14), 5066–5076 (2022) https://doi.org/10.1080/10298436.2021.1993219

[19] Liu, F., Al-Qadi, I.L.: Physics-informed graph neural network for 3D spatiotemporal structural response modeling of flexible pavements. Engineering Applications of Artificial Intelligence **162**, 112391 (2025) https://doi.org/10.1016/j.engappai.2025.112391

[20] Cardoso Da Silva, D., Rakotovao Ravahatra, N., Picoux, B., Reynaud, P., Yotte, S., Petit, C.: Parameter uncertainty and statistical analysis of tyre-pavement interaction under braking. Road Materials and Pavement Design **26**(sup1), 263–289 (2025) https://doi.org/10.1080/14680629.2025.2483480

[21] Wallace, E.R., Chaise, T., Nelias, D.: Three-dimensional rolling/sliding contact on a viscoelastic layered half-space. Journal of the Mechanics and Physics of Solids **143**, 104067 (2020) https://doi.org/10.1016/j.jmps.2020.104067

[22] Kalker, J.J.: Three-Dimensional Elastic Bodies in Rolling Contact, 1st edn. Solid Mechanics and Its Applications, vol. 2. Springer, Delft-Rotterdam (1990)

[23] Gallego, L., Nelias, D., Deyber, S.: A fast and efficient contact algorithm for fretting problems applied to fretting modes I, II and III. Wear **268**(1), 208–222 (2010) https://doi.org/10.1016/j.wear.2009.07.019

[24] Wallace, E.R., Chaise, T., Duval, A., Nelias, D.: Transient tractive rolling contact between elastically dissimilar and multi-layered bodies. International Journal of Solids and Structures **265–266**, 112124 (2023) https://doi.org/10.1016/j.ijsolstr.2023.112124

[25] Yu, C., Wang, Z., Wang, Q.J.: Analytical frequency response functions for contact of multilayered materials. Mechanics of Materials **76**, 102–120 (2014) https://doi.org/10.1016/j.mechmat.2014.06.006

[26] Oubahdou, Y.: Etude expérimentale et rationnelle de la dégradation des couches de surfaces de chaussées. Thesis, Université de Limoges, Limoges, France (2022)

[27] Nélias, D., Antaluca, E., Boucly, V., Cretu, S.: A Three-Dimensional Semianalytical Model for Elastic-Plastic Sliding Contacts. Journal of Tribology **129**(4), 761–771 (2007) https://doi.org/10.1115/1.2768076

[28] Mazars, J.: A description of micro- and macroscale damage of concrete structures. Engineering Fracture Mechanics **25**(5-6), 729–737 (1986) https://doi.org/10.1016/0013-7944(86)90036-6

[29] Cardoso Da Silva, D., Rakotovao Ravahatra,

N., Picoux, B., Reynaud, P., Yotte, S., Petit, C.: Semi-analytical modelling of realistic tire-pavement contact: An analysis of pavement surface cracking damage under critical driving conditions. Road Materials and Pavement Design **26**(4), 1008–1031 (2024) https://doi.org/10.1080/14680629.2024.2386017

[30] Corté, J., Guidoux, Y.: Catalogue des Structures Types de Chaussées Neuves. SETRA-LCPC, Bagneux, Paris (1998)

[31] Mitrovich, J., Maddipatla, S.S.P., Gao, L., Guler, I., Beal, C., Brennan, S.: Analysis of Friction Utilization Within a Roadway Network Using Simulated Vehicle Trajectories. In: 2023 IEEE Conference on Control Technology and Applications (CCTA), pp. 905–910. IEEE, Bridgetown, Barbados (2023). https://doi.org/10.1109/CCTA54093.2023.10253155

[32] Regulation No 13 of the Economic Commission for Europe of the United Nations (UN/ECE) — Uniform Provisions Concerning the Approval of Vehicles of Categories M, N and O with Regard to Braking [2016/194] (2016)

[33] SETRA-LCPC: Guide technique de conception et dimensionnement des structures de chaussée (1994)

[34] Myers, R.H., Montgomery, D.C., Anderson-Cook, C.M.: Response Surface Methodology, 3rd edn. Wiley Series in Probability and Statistics. Wiley, ??? (2009)

[35] Hamada, M., Wu, C.F.J.: Analysis of Designed Experiments with Complex Aliasing. Journal of Quality Technology **24**(3), 130–137 (1992) https://doi.org/10.1080/00224065.1992.11979383

[36] Sobol, I.M., Kucherenko, S.: Derivative based global sensitivity measures. Procedia - Social and Behavioral Sciences **2**(6), 7745–7746 (2010) https://doi.org/10.1016/j.sbspro.2010.05.208

[37] McKay, M.D., Beckman, R.J., Conover, W.J.: Comparison of Three Methods for Selecting Values of Input Variables in the Analysis of Output from a Computer Code. Technometrics **21**(2), 239–245 (1979) https://doi.org/10.1080/00401706.1979.10489755